Measurement of Flow Field in Biofilm Reactors by 3-D Magnetic Resonance Imaging

Kevin P. Nott, Frank P. Heese, and Laurance D. Hall
Herchel Smith Laboratory for Medicinal Chemistry, University of Cambridge School of Clinical Medicine, University Forvie Site, Robinson Way, Cambridge, CB2 2PZ, U.K.

Lynne E. Macaskie and Marion Paterson-Beedle
School of Biosciences, University of Birmingham, Edgbaston, Birmingham, B15 2TT, U.K.

DOI 10.1002/aic.10537
Published online August 29, 2005 in Wiley InterScience (www.interscience.wiley.com).

3-D Magnetic resonance imaging (MRI) was used to measure the flow field of water in a packed-bed column containing Serratia sp. biofilm supported on polyurethane foam, and subsequently to follow a reaction which precipitates lanthanum phosphate on the biofilm. Sensitizing the MR image contrast to the fluid flow along the axis of the bioreactor provided better image-contrast between the foam and fluid compared to that based on MR signal intensity alone. After reaction, that same "velocity contrast" effectively defined the difference between blocked and unblocked regions by distinguishing between regions of flow and no flow. Data acquired during progressive blockage of reactors challenged at two different flow rates accord with reactor theory; thus, the faster flow rate replenished the reactants uniformly, whereas at the slower flow rate the reactants were concentration limited. MRI velocimetry was used to generate data that can be used to model reactors where the efficiency is progressively compromised by blockage due to precipitation. © 2005 American Institute of Chemical Engineers
AIChE J, 51: 3072–3079, 2005
Keywords: MRI, serratia, bioreactor, flow, blockage

Introduction

With increasing environmental legislation concerning the release of industrial wastewaters, there is a growing need for efficient and economical remediation methods to treat such fluids. It is encouraging, therefore, that there is an increasing body of evidence to suggest that microorganisms can be used for the removal of heavy metals from industrial effluents which can be detrimental to health.[1,2] Thus, an effective method has been developed that can typically remove 85–95% of heavy metal ions by passage through a bioreactor containing immobilised *Citrobacter* biofilm;[3] a cell-bound phosphatase liberates inorganic phosphate from an organic "donor" molecule, which then promotes the formation of cell-bound metal phosphate.[4] A simple model has been derived from the Michaelis-Menten equation to relate the efficiency of removal of metal ions[5,6] from a uranium mine wastewater semiquantitatively to the input flow rate, total enzyme loading and bioreactor activity.[6] However, that model assumes ideal plug-flow behavior and is limited to bulk parameters that describe the overall reactor performance, and cannot account for the spatial and temporal changes in flow field induced by blockage formation. Although assumption of ideal plug-flow behavior is generally fundamental to fixed-bed bioreactor modeling, that assumption is difficult to prove experimentally within the 3-D dynamic system of an operational flow-through reactor. Use of controlled blockage deposition does provide a tool whereby these factors can be investigated quantitatively, but that "black box" approach based on analysis of input- and exit-solutions, provides no spatio-temporal information, and, hence, is of little use in process optimization.

It is known that MRI is a powerful tool that can measure, noninvasively, the velocity of opaque fluids in three dimen-

Correspondence concerning this article should be addressed to K. P. Nott now at kevin.nott@oxinst.co.uk.

sions, and, hence, it is invaluable for many process engineering applications.[7–9] Increasingly, MRI is also being used for environmental engineering and biotechnology applications.[10,11] Of specific relevance to this study, MRI has previously been used to visualise the formation of biofilm as well as the flow velocity of fluid in a bioreactor cell;[12–16] it has also been used to follow the absorption of heavy metals in alginate, immobilised cells and algal biosorbents.[17–20]

As part of a broad ranging study using noninvasive imaging techniques to investigate the function of a biofilm bioreactor, it has already been demonstrated that MRI of the aqueous medium can visualize biofilm on polyurethane reticulated foam, as well as the removal of Cu^{2+}/La^{3+} ions by biosorption and inorganic precipitation.[21] This is possible because the MR properties of water protons are dependent on the concentration and molecular environment of the water molecules. Thus, heavy metal ions (La^{3+}) induce a concentration-dependent relaxivity, or in the case of paramagnetic ions (Cu^{2+}), a susceptibility effect which alters the MR properties of vicinal water molecules, and thereby provides image contrast with the bulk of the aqueous medium. Extensive phosphatase-mediated bioaccumulation of $LaPO_4$ was observed, but no evidence for deposition of $Cu_3(PO_4)_2$ was obtained by X-ray diffraction and proton-induced X-ray emission analyses;[21] those observations were confirmed by MRI. Since Cu^{2+} was not taken up into the biofilm it was concluded that Cu^{2+} could be added as an MRI contrast agent to increase signal-to-noise from the perfusate during experiments to monitor the biodeposition of $LaPO_4$, which shows as regions of low signal intensity because of the lack of water. On that basis, it was decided that this is a good model system for a noninvasive study of the function of a biofilm reactor by MRI velocimetry; in turn, that prompted the present study, which seeks to answer the following questions:

(1) Can MRI quantitate in three dimensions the entire 3D flow velocity field of fluid flowing through the reactor?

(2) If so, are such data sensitive to the progressive deposition of metal as it is removed from the wastewater stream?

(3) What are the effects of the air bubbles entrained in the support matrix on the fluid flow, and is it possible to distinguish them from the metal precipitate?

(4) Can MRI be used to generate data to refine the existing enzyme kinetic-based model, and hence help the design of a more efficient reactor?

Flow Imaging

The theory of MRI and its application to the study of a biofilm reactor has been described previously.[22] MRI of water is based on the spatial localization of the nuclear magnetic resonance (NMR) signal in a homogeneous magnetic field via the application of linear magnetic field gradients. If, in addition to those spatial encoding gradients, a pair of gradient pulses with strength g, both with duration δ and separated by Δ are applied in a particular direction, the phase of the MRI signal is sensitised to flow in that direction;[23–25] a typical pulse sequence as used in this study is shown in Figure 1. The phase ϕ, of the signal at each pixel of the resulting pulsed field gradient (PFG) velocity-encoded MR image is related to velocity v, by the equation

$$\phi = \gamma\delta g\Delta v + \Theta$$

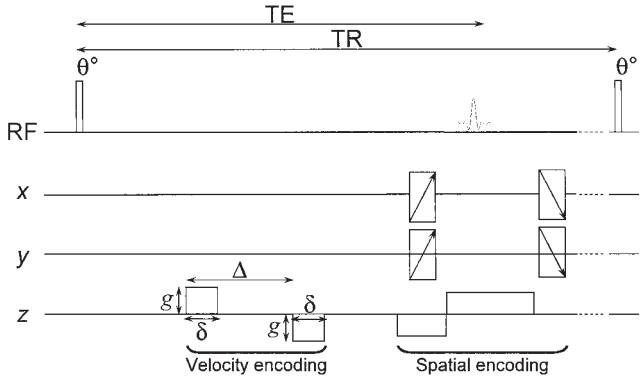

Figure 1. Gradient echo imaging sequence with interleaved Pulsed Field Gradient (PFG) pair.

Each radio frequency (RF) pulse tips the magnetisation of the water protons through a flip angle θ°, and its magnitude and phase are recorded at the end of the "echo time" (TE). TE is set to reflect the spin-spin relaxation time (T_2) of the protons; the shorter the T_2, the shorter must be TE. Successive RF pulses are separated by the "repetition time" (TR), which is long enough for the magnetisation to relax fully before the next RF pulse is applied. 3-D spatial encoding is achieved by using a fixed z gradient whilst incrementing the x and y gradients; thus, the total scan time is $N_x \times N_y \times$ TR, where N_x and N_y are the number of pixels in the x and y directions respectively. Velocity encoding is achieved by application of a bipolar gradient pair, in this example in the z direction parallel to the bulk flow.

where γ is the magnetogyric ratio of the ^{1}H nucleus and Θ is the phase offset caused by any magnetic field inhomogeneity. Therefore, a series of images can be acquired with different gradient strengths to obtain a value of flow velocity for each pixel. Velocity images can be acquired sequentially for all three orthogonal (x, y, z) directions, where required, to provide the complete 3-D flow field.

Experimental

Preparation of Reactor Packed-Bed Systems for Metal Removal by Serratia Biofilm

Citrobacter sp. NCIMB 40259, now reassigned to the genus *Serratia* by modern molecular and biochemical methods,[26] was used under licence from Isis Innovation (Oxford, U.K.). The conditions for controlled growth of *Serratia* sp. biofilm have been established.[4] The biofilm was grown on polyurethane reticulated foam (Filtren TM 30 cubes, 1 cm^3) supplied by Recticel (Belgium) in an air-lift fermenter in continuous culture, as described previously.[4] The reticulated foam cubes, coated with biofilm of average thickness of 26 μm[27] were withdrawn after six days of continuous culture. The phosphatase specific activity of the cells from the fermenter was determined by the release of *p*-nitrophenol (PNP) from *p*-nitrophenyl phosphate (PNPP); one unit is defined as nmol PNP liberated per min per mg bacterial protein.[4] In all experiments resting cells were used since no further growth medium was provided; effectively the biofilm behaves as an immobilising matrix for the phosphatase enzyme.

All measurements were made using cylindrical glass columns (16 mm dia., 70 mm length) packed, without compression, with 88, 0.125 cm^3 cubes of polyurethane foam with

immobilised *Serratia* sp. biofilm[21] (made by dividing 1 cm^3 cubes obtained from the fermenter into eight).

MRI Velocity Measurements

All ^1H MRI images were acquired using a Bruker MSL-100 imaging console (Bruker Analytische Messtechnik GmbH, Karlsruhe, Germany) operating under TOMIKON software (Bruker Medizintechnik GmBH., Karlsruhe, Germany) connected to an Oxford Instruments 2 Tesla, 31 cm horizontal bore super-conducting magnet (Oxford, U.K.). The 11 cm internal dia. gradient set and radio-frequency (RF) probe (internal dia. 5.5 cm) were built "in house." Each axis of the gradient set was powered by two Techron® amplifiers (Models 7560 and 7570, Elkhart, IN, U.S.A.) giving gradient strengths up to 195 mT/m. The data were transferred to a Linux workstation and processed into images using CaMReS software written by Dr. N. J. Herrod.

3-D dimensional flow encoded images (256 × 64 × 64 pixels) were acquired using a PFG gradient echo sequence (TR/TE/θ 100 ms/7.5 ms/90°) with 312.5 μm isometric spatial resolution in a scan time of 6 min 50 sec; a schematic is given in Figure 1. A total of ten images was acquired, with five different velocity encoding gradient strengths (−117, −19.5, 0, +19.5, +117 mT/m), with and without flow, giving a total scan time of 1.1 h for each velocity direction either transverse (x and y) or parallel (z) to the bore of the magnet. The fluid flow was provided by an electromagnetically driven gear pump (Integral Series 120 pump, Micropump Inc., Vancouver, WA) which was used to replenish water in a constant head gravitational flow vessel held at a given height in order to provide the reactor with steady-state flow. The velocity encoded images acquired without flow were used to correct for errors caused by imperfections in the motion encoding gradients. Initially x, y, and z velocity measurements were carried out on a bioreactor containing foam cubes with biofilm, using a 20 mM $CuSO_4$ solution to enhance the signal-to-noise of the experiment and consequently the accuracy of the velocity measurement. Concentrations normally toxic to the biofilm could be used since no biomass growth was required and the probe solution was recycled without any consequence to the remaining experiment. The velocity-encoded images were processed using a Bayesian statistical method for analysis in order to maximize accuracy over a wider range of velocities using fewer gradient steps.[28]

Bioreactor Challenge Experiments

Metal accumulation was achieved using two "fresh" columns side-by-side inside the magnet as shown in Figure 2, and challenged with a fluid containing La $(NO_3)_3 \cdot 6H_2O$ (1 mM; for lanthanum phosphate precipitation onto the biomass), $CuSO_4 \cdot 5H_2O$ (1 mM; not precipitated appreciably onto the biomass[21]), and sodium glycerol-2-phosphate (5 mM; phosphate donor) in sodium citrate buffer (2 mM; to prevent metal hydrolysis and maintain metal solubility in the input solution), pH 6.0. Two different flow rates (11 and 128 ml/hr, hereafter termed "slow" and "fast" flow) were generated by an external peristaltic pump (Watson-Marlow, 505U, Wilmington, MA); these conditions were chosen, using data from outflow analyses in preliminary tests, to give contrasting results; in the absence of obstructions those would have Reynolds numbers (N_{Re}) of 0.25 and 2.87, respectively. The Peclet numbers for the reactors at the slow and fast flow rates are ca. 22 and 261, respectively, both calculated from the equation $Pe = UL/D_a$ where: U is the average velocity; L the pore size of the foam; and, D_a is the dispersion coefficient.[29] Initially the columns were challenged for two hours to allow La^{3+} and Cu^{2+} ions to be background-absorbed onto the biofilm. Subsequently, MRI velocity measurements were made under constant head gravitational flow; 1 mM $CuSO_4$ solution was used in order to maximise the signal-to-noise and consequently the accuracy of the measurement, without being toxic to the phosphatase enzyme (necessary for the next metal accumulation phase); the effluent was not recycled to prevent recirculation of any biofilm cells which had sloughed off. The flow rate used was over 100 times faster than that for the La^{3+} supplemented solution, in order to produce velocities which were measurable by MRI, but also too high for the metal deposition reactions to occur during the flow residence time. The flow rate was measured gravimetrically at the outlet pipe, and was maintained at approximately 3120 ml/h in both reactors for all the flow measurements; this corresponds to a Reynolds number (N_{Re}) of 70 without any obstructions. Importantly, since the flow data are acquired over many hours it was important to ensure that the flow is steady and non turbulent to enable measurement of velocity.

Subsequently, the reactors were challenged for three longer periods (each ca. 20 h) each followed by MRI velocity measurements to spatially probe the progressive blockage (256 × 128 × 64 pixels for both reactors, giving a total acquisition time 2.3 h). The time-dependent precipitation of lanthanum phosphate was also monitored by analysis of bioreactor outflows using spectrophotometry (see later).

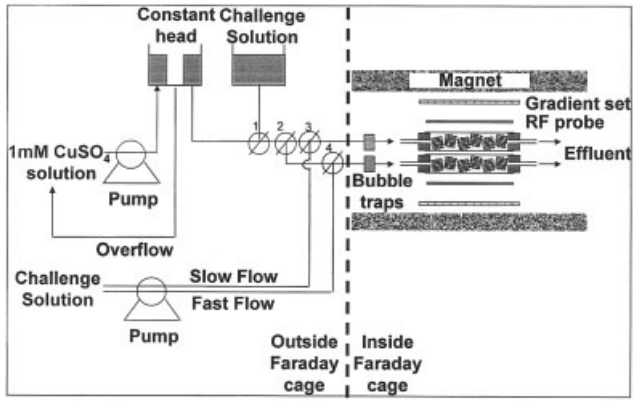

Figure 2. Continuous experiment carried out *in situ* in the magnet.

Once the scanner had been tuned with the reactors inside the RF probe, the experimental conditions could be controlled sequentially. Initially, the challenge solution was pumped through two reactors at different flow rates (11 and 128 ml/h, termed "slow" and "fast") for a 2 h period; that solution was then displaced by 1 mM aqueous $CuSO_4$ for measurement of the flow velocity over the next 2.3 hr. Subsequently, this fluid was displaced using a reservoir of challenge solution and the "slow" and "fast" flows of challenge solution restored for a further defined period (ca. 20 h) before a second set of velocity measurements based on the $CuSO_4$ solution. This cycle was repeated two more times to effectively create a 4-D data set of the time dependence of the 3-D spatial effects.

Spectrophotometric Analyses of La^{3+}, Cu^{2+} and Inorganic Phosphate

The La^{3+}, Cu^{2+} and phosphate contents of the outflows of the reactors were measured as described by Yong and Macaskie,[30] Nott et al.,[21] and Yong and Macaskie,[31] respectively.

Environmental Scanning Electron Microscopy

Samples of *Serratia* sp. biofilm grown on polyurethane reticulated foam with and without lanthanum phosphate deposits were visualized using environmental scanning electron microscopy (ESEM) (FEI Philips FEG ESEM XL30) in their hydrated state. The samples containing lanthanum phosphate were taken from a "slow" reactor.

Magnitude Data Analysis

Whereas the phase of the MRI signal was sensitized to velocity, the magnitude of the MRI signal acquired simultaneously, is primarily dependent on water proton density. Hence, the blockage could be quantitated using the magnitude of the MRI image acquired without either flow or flow encoding, by segmenting high signal intensity from the challenge solution from that of any obstructions, such as the foam, biofilm, precipitate and/or air bubbles (low signal intensity). The cut off intensity was chosen to be 25% of the maximum signal intensity from the challenge solution, and each data set was referenced against the first, which had no appreciable blockage despite the two hours exposure to the La^{3+} supplemented solution.

Flow Data Analysis

In general, 15% of the length of the MR images at either end of the reactor was unusable for quantitative analysis of the flow data because the magnetic field homogeneity in those regions was poor. In addition, it is apparent from a preliminary study using sagitally orientated slices (Figure 3) that the available gradient linearity (magnetic field strength vs. position) was poor. Thus, although the transverse image dimensions were circular across the bioreactor, the MRI sagittal image along its length was distorted towards the inlet and outlet. Consequently, the cross-sectional area, required for calculation of the average z velocity (including zeros), had to be determined separately from each slice using the following procedure programmed using Matlab (Mathworks Inc., Natick, U.S.A.):

(1) The centers of the circular transverse images at each end of the usable region (central 70% of the length) were defined manually.

(2) An imaginary straight line was drawn between them to define the center of the intervening slices.

(3) For each transverse slice, starting from the estimated center, the size of a circle was increased until it had the largest radius (that is, the maximum distance) which included a non zero velocity pixel.

(4) For each of the resultant circular regions-of-interest (ROI's) including areas of zero velocity, the average z velocity V_{avg} was calculated; separately the areas of zero velocity were excluded for estimation of the non stagnant average z velocity V_{ns}.

(5) The blockage fraction (BF) was calculated using the equation, $1 - V_{avg}/V_{ns}$.

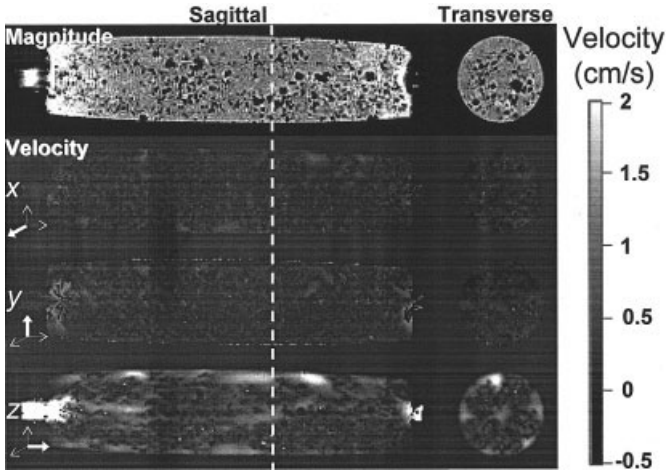

Figure 3. Sagittal and transverse MRI images.

Sagittal and transverse images (taken at the position of the dotted line) of water in a reactor containing biofilm immobilised on foam cubes. The pair of upper traces was taken from a 3-D data set of signal magnitude and shows the spatial distribution of water. The image intensity in the lower three traces has been sensitised to the flow velocity in the x-, y- and z-directions.

Results

Figure 3 shows sagittal and transverse slice images taken from the 3-D data sets of signal magnitude (related to water distribution), plus the x, y, z vectorial velocity taken from three separate phase encoded 3-D maps of fluid flow through a reactor before treatment. The heavy Cu^{2+} doping (20 mM) dominates the relaxation behavior of water protons in both the biofilm and surrounding fluid, hence, there is little contrast in the signal magnitude image compared to a previous study;[21] in fact the upper image resembles that of reactor with no biofilm and visualizes the small and large voids associated with the foam and air bubbles, respectively. Although the x and y velocities were too low to be measured accurately, and the foam structure is not clearly discernible than for z, the z velocity image is very sensitive to the foam structure. The highest z velocities are found in the gaps between the foam cubes which disperse the high velocity jet as it enters the bioreactor; the fluid then follows the path of least resistance and channels between the foam cubes and down the sides. Since neither the x nor y components provided additional information, all subsequent velocity measurements were carried out only in the z-direction, parallel to the direction of flow; this reduced the total scan time for the flow measurements from 6.8 to 2.3 h.

Figure 4 shows specimen data of the concentrations of lanthanum, copper and phosphate ions and the pH during challenge by an aqueous solution of lanthanum nitrate (1 mM), copper sulphate (1 mM) and sodium glycerol-2-phosphate (5 mM) in a sodium citrate buffer (2 mM), pH 6.0 at the two different flow rates; samples were taken from the outflow before each imaging experiment. As was found previously,[21] under both conditions the concentration of copper ions in the outflow was 1 mM indicating little or no copper removal. In contrast, the majority of the La^{3+} was removed by both the "fast" and "slow" flow reactors. The pH in both reactors increased in the latter half of the experiment. Thus, the "slow"

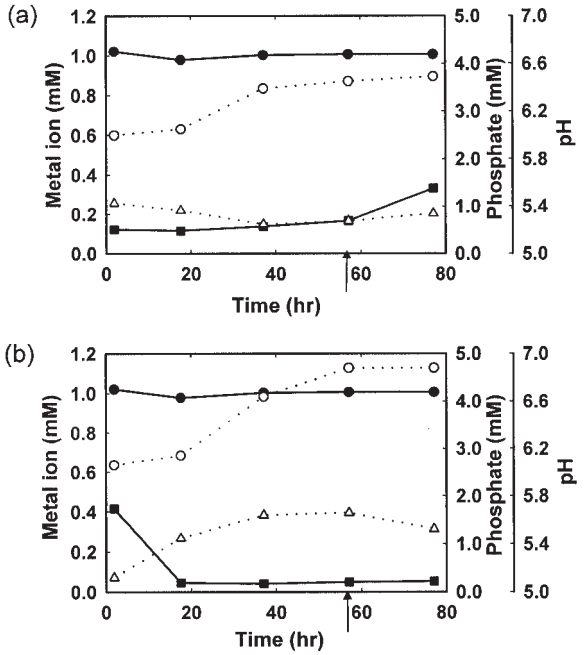

Figure 4. Phosphate-release and metal-removal by reactors.

Challenged at (a) 128 ml/h (fast), and (b) 11 ml/h (slow) flow with aqueous La^{3+} (1 mM) and Cu^{2+} (1 mM) in the presence of glycerol-2-phosphate (5 mM) and citrate buffer (2 mM), pH 6.0. ● = Residual Cu^{2+}. ■ = Residual La^{3+}. △ = Phosphate released. ○ = pH of outflow solution. The arrow indicates the time (57.1 h) at which the concentration of free phosphate species were estimated.

reactor gave 1.65 mM phosphate in the outflow (at 57.1 h) and a higher pH upshift (6.00 to 6.88) whereas the "fast" reactor gave 0.69 mM phosphate in the outflow (at 57.1 h) and, a smaller pH upshift (6.00 to 6.45). This can be explained by the reaction of the PO_4^{3-} ion generated by the system, that is, cleaved from the disodium glycerol 2-phosphate, with water initially to form HPO_4^{2-} and then $H_2PO_4^-$, as follows

$$PO_4^{3-} + H_2O \leftrightarrow HPO_4^{2-} + OH^- \quad (1)$$

$$HPO_4^{2-} + H_2O \leftrightarrow H_2PO_4^- + OH^- \quad (2)$$

The basic dissociation constants for Eqs. 1 and 2 are $K_{b1} = 2.22 \times 10^{-2}$ and $K_{b2} = 1.58 \times 10^{-7}$, respectively.[32] In this case $K_{b1} \gg K_{b2}$, therefore, essentially all the OH^- arises from the first reaction. The fractions (α) of HPO_4^{2-} and $H_2PO_4^-$ at pH 6.45 and 6.88 were determined using the plot of distribution of various phosphate species (α) as a function of pH.[33] The estimated concentrations of the phosphate species ([phosphate-containing species] = $\alpha \times$ total phosphate concentration) in the outflow of the "slow" reactor were $[HPO_4^{2-}] = 0.54$ mM and $[H_2PO_4^-] = 1.11$ mM, and in the "fast" reactor were $[HPO_4^{2-}] = 0.11$ mM and $[H_2PO_4^-] = 0.58$ mM. Thus, the "slow" reactor, with a higher pH in the outflow, contains a higher concentration of HPO_4^{2-} species in solution than does the "fast" reactor.

During metal accumulation, all the "slow" reactor columns showed a heavy deposition near the inlet, whereas with the "fast" reactors this was more evenly dispersed along the length of the column. This is to be expected since the bulk of the substrate cleavage, and hence metal precipitation, would occur near the reactor inlet at slow flow rates; in contrast, at faster flows more unreacted substrate can pass to the column's distal areas, thereby giving a more even distribution of precipitate and hence less local blockage. Figure 5 shows ESEM micrographs of *Serratia* sp. biofilm containing lanthanum phosphate deposits taken from a "slow" reactor. The blockage fraction accumulated during the experiment was measured at three different times by thresholding the magnitude MR-images of both the "fast" and "slow" flow reactors. The results in Figure 6 show that even in the early stages precipitation was more uniform in the "fast" flow reactor (Figure 6a), whereas the "slow" flow reactor showed preferential blocking at the inlet

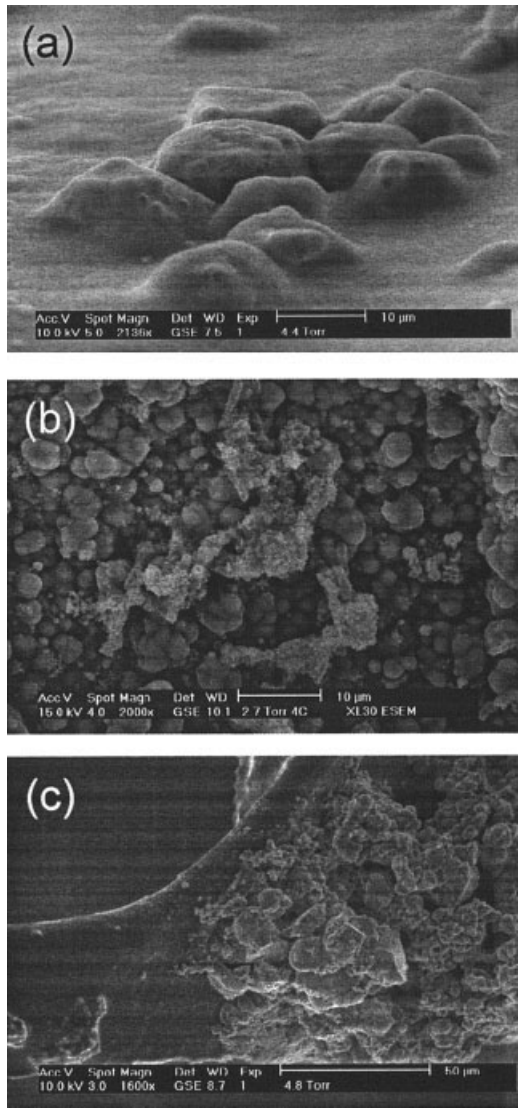

Figure 5. ESEM micrographs.

(a) *Serratia* sp. biofilm on reticulated polyurethane foam (2136 magnification), and samples of *Serratia* sp. biofilm on reticulated foam containing lanthanum phosphate deposits taken from: (b) the middle (2000 magnification), and (c) the bottom (1,600 magnification) of a "slow" reactor.

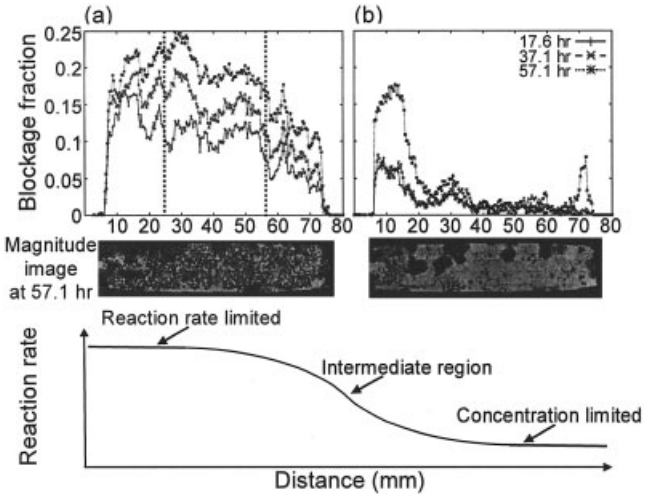

Figure 6. Blockage fraction within the reactor as a function of time.

Each of the 2-D slice images was taken from a 3-D magnitude image after 57.1 h of flow either at (a) 128 ml/h (fast), and (b) 11 ml/h (slow). The blockage fractions were calculated by thresholding the signal intensities for scans measured at 17.6, 37.1 and 57.1 h after initiation. All of the data are in good accord with reactor theory: thus, the "fast" reactor is more efficient with the reactants distributed uniformly, whereas the "slow" reactor is concentration limited.

region, which was particularly pronounced after 57 h (Figure 6b).

The "fast" flow rate was chosen, by prior experiment, as that which gave a small amount of La^{3+} in the outflow solution (that is, the threshold value at which not all of the La^{3+} was removed within the flow residence time). Thus, La^{3+} was removed to >95% at the slow flow rate (Figure 4b), but only ca. 90% at the fast flow rate (Figure 4a); the corresponding phosphate concentrations found in the flow were ca. 1.7 mM and 0.7 mM; at the slow flow rate more glycerol 2-phosphate cleavage occurred within the flow residence time. Figure 7 shows plots of the values of the non stagnant average z velocity (V_{ns}), average z velocity (V_{avg}), and blockage fraction (BF) for the central section of the "fast" flow reactor; there was little variation in the same region of the "slow" reactor for further analysis (blockage was largely confined to the post-inlet region). In theory, V_{avg} should be the same for each transverse slice across the reactor; however, in practice this was not the case, probably due to the presence of the air bubbles which distorted the image, especially the phase data used to calculate the flow velocity. However, since V_{avg} and V_{ns} are both calculated using the same region of interest, each acts as an internal reference for the other, and, hence, these fluctuations cancel out because the air bubbles are stable throughout each 2.3 h experiment. The data show clearly the development of blockages with time in the 7 mm and 28 mm regions (Figure 7c).

These data are further quantified in Figure 8, which shows the correlation between blockage fraction and non stagnant average z velocity for the data given in Figure 7, with pooled data from two replicate experiments. The curve was fitted to the equation $BF = 1 - V_{avg}/V_{ns}$; hence, the intercept on the V_{ns} axis when $BF = 0$ equates to V_{avg} and the value of 0.47 cm/s is the same as that obtained by volumetric analysis. The wide spread of data is because the signal-to-noise of MRI is poor on a pixel-to-pixel basis; however, using the pixels collectively increases the signal-to-noise and, as a consequence, the confidence of the measurements as a whole.

Discussion

These experiments demonstrate the potential utility of MRI not only in this specific application, but for many other processes which take place in columnar reactors, for which the resultant efficiency is changed by blockage; for example, filtration. The image data can provide significant information regarding the spatial distribution of blockage caused a by

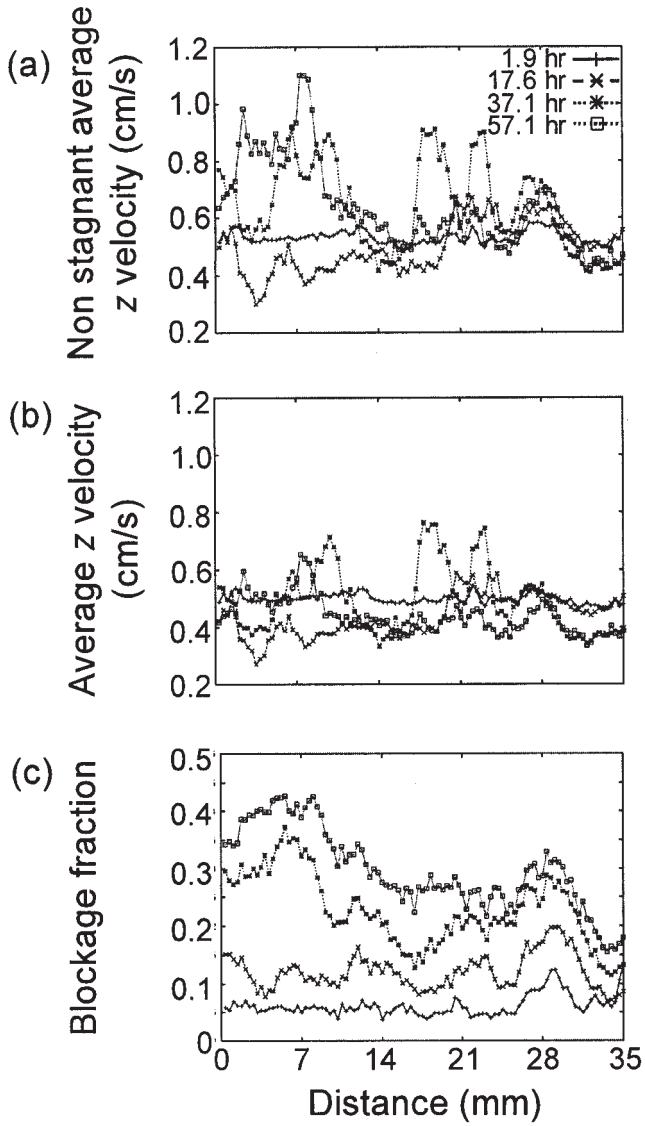

Figure 7. Sample data from a representative MRI velocimetry experiment for the "fast" reactor.

Plots of: (a) Nonstagnant average z velocity, V_{ns}; (b) average z velocity, V_{avg}, and (c) blockage fraction, $BF\ (=1 - V_{avg}/V_{ns})$, calculated using each slice, transverse to the direction of the flow, along the length of the reactor taken from the 3-D data set. Although in theory, V_{avg} in (b) should be the same for each slice along the reactor, in practice this was not the case. However, V_{ns} which was calculated in (a) using the same region of interest, showed similar fluctuations which cancel out for the calculation of BF shown in (c).

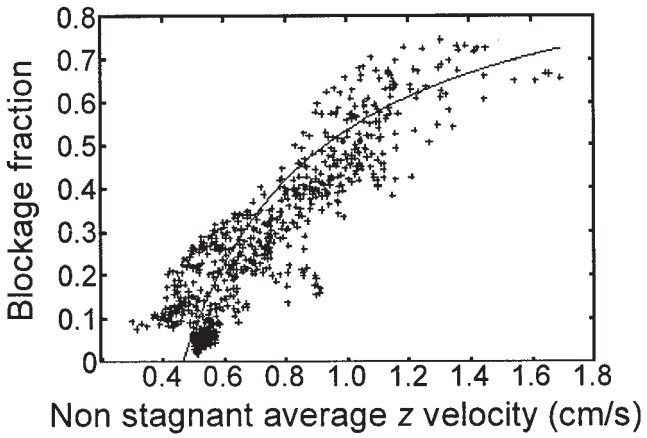

Figure 8. Correlation between non stagnant average *z* velocity and blockage fraction.

This correlation is based on the combined data from two independent experiments at the fast flow rate.

progressive reaction, which could not otherwise be gathered from analysis of the bulk outflow (the "black box" approach) or be visualized by eye through the opaque precipitate. In the case of an enzymatic reaction the local flow residence "time" is critical since the reaction is time dependent; static flow in stagnant areas "wastes" capacity, whereas rapid flow in others would allow insufficient time to retain V_{max} (maximum reaction velocity) locally. The overall bioreactor activity is defined to relate to the concentration of substrate and available biomass,[5,6] but only at a constant flow rate which maintains the local substrate concentration high enough to maintain V_{max} throughout.

Analysis of the concentration of La^{3+}, Cu^{2+}, and phosphate ions as well as the pH of the outflow solution from the "fast" and "slow" flow reactors showed some differences (Figure 4); however, one cannot predict from those data how efficient the reactors will be in the longer term. Even after the first day, the signal magnitude of the MR image reveals that the "fast" reactor is more efficient overall since the reactants, and, hence, as a consequence the precipitate, are both more uniformly distributed; however, in contrast the "slow" reactor is concentration limited since it cannot replenish the reactants fast enough along the length, which leads to blockage at the inlet. That this combination of results is in accord with reactor theory, is well illustrated in Figure 6. The MR images also reveal the presence of air bubbles which cannot be observed directly by eye, yet are clearly distinguished as zero signal intensity regions compared to the grey scale appearance of the precipitate.

In contrast to "thresholding" of the magnitude images which can be subjective, MRI quantitation of flow through the reactors not only defines the difference between blocked and unblocked regions by distinguishing regions of flow and no-flow, but the resultant "velocity contrast" is also sensitive to smaller obstructions, such as the foam. Areas of apparent zero velocity include features, such as air bubbles; however, it is important to note that since those images may also include areas where the signal-to-noise is not sufficient to support the Bayesian analysis of the velocity encoded images (that is, below the signal-to-noise threshold), they will tend to overestimate extent of the blockage. In the present study, comparison of the blockage fraction across the "fast" flow reactor calculated from the velocity data (Figure 7c) with that from the equivalent region of the MR magnitude image (between the dotted lines in Figure 6a) shows that although the precise values are different, the peaks and troughs are similar.

If the overall bulk flow rate through the reactor vessel is constant throughout the duration of the experiment, then the average velocity V_{avg}, should remain the same for each transverse slice across the reactor. However, local blockage within any one region will cause the flow to be constricted to smaller areas causing the non stagnant average z velocity, V_{ns}, to increase. This is clearly demonstrated in Figure 8 which shows a progressive increase in flow velocity and a quantitative relationship with blockage.

Conclusions

This study clearly demonstrates that MRI can quantitate the flow field in a biofilm reactor, distinguishing the lower velocity flow within the polyurethane reticulated foam cubes from the higher velocity flow between them, and along the inner edges of the reactor tube. Flow imaging is also sensitive to the buildup of metal precipitate, and, hence, enables quantitation of the blockage fraction; however, it is not possible to distinguish air bubbles from the precipitate by flow data alone since both regions are characterised by zero flow. The experimental data already available from this study are reminiscent of "text book" theory, and, hence, in principle, could be used to model and subsequently to optimize the efficiency of this biofilm reactor for scaleup. Further data could be acquired to refine the current model, developed from applied enzyme kinetics, which assumes ideal plug flow, or that the deviations from ideal behavior are constant throughout, and that the value of the K_m of enzymes in immobilized bacteria ($K_{m\ apparent}$) is a constant.[5,6,34] That the former is not the case is clearly demonstrated by the radial profiles taken along the biofilm reactor with increased blockage; the adjacent local flow rate is increased, and, hence, the amount of substrate which flows past the enzyme is a variable parameter, the value of which depends on the extent of local blockage and the exact position of each enzyme molecule in the reactor. Future models need to take this into account and further refinements of the MRI technique and subsequent data analysis may be required for future studies of such systems.

Acknowledgments

This work was supported by the U.K. Biotechnology and Biological Sciences Research Council (Grant Nos. EO9214 and 6/E1464), and by the Herchel Smith Endowment. The authors thank Recticel (Belgium) for the biofilm support. KPN, FPH and LDH would like to thank Dr. N. J. Herrod and Dr. D. Xing for the computer software and facilities, respectively; and Richard Smith, Simon Smith and Cyril Harbird for supply and maintenance of the MR, and other hardware.

Literature Cited

1. Alexander M. Biodegradation and bioremediation. San Diego: Academic Press, 1999.
2. Valls M, de Lorenzo V. Exploiting the genetic and biochemical capacities of bacteria for the remediation of heavy metal pollution. *FEMS Microbiology Reviews.* 2002;26:327–338.
3. Macaskie LE. An immobilized cell bioprocess for the removal of heavy metals from aqueous flows. *J of Chem Technol and Biotechnol.* 1990;49:357–379.

4. Finlay JA, Allan VJM, Conner A, Callow ME, Basnakova G, Macaskie LE. Phosphate release and heavy metal accumulation by biofilm-immobilized and chemically-coupled cells of a *Citrobacter* sp. pre-grown in continuous culture. *Biotechnol and Bioeng.* 1999;63:87–97.
5. Macaskie LE, Empson RM, Lin F, Tolley MR. Enzymatically-mediated uranium accumulation and uranium recovery using a *Citrobacter* sp immobilized as a biofilm within a plug-flow reactor. *J of Chem Technol and Biotechnol.* 1995;63:1–16.
6. Macaskie LE, Yong P, Doyle TC, Roig MG, Diaz M, Manzano T. Bioremediation of uranium-bearing wastewater: biochemical and chemical factors influencing bioprocess application. *Biotechnol and Bioeng.* 1997;53:100–109.
7. Gladden LF. Nuclear-magnetic-resonance in chemical-engineering—principles and applications. *Chem Eng Sci.* 1994;49:3339–3408.
8. Gladden LF, Alexander P. Applications of nuclear magnetic resonance imaging in process engineering. *Measurement Sci and Technol.* 1996; 7:423–435.
9. Gladden LF. Applications of in situ magnetic resonance techniques in chemical reaction engineering. *Topics in Catalysis.* 1999;8:87–95.
10. Lens PNL, Hemminga MA. Nuclear magnetic resonance in environmental engineering: principles and applications. *Biodegradation.* 1998;9:393–409.
11. Van As H, Lens P. Use of ^{1}H NMR to study transport processes in porous biosystems. *J of Ind Microbiol and Biotechnol.* 2001;26:43–52.
12. Lewandowski Z, Altobelli SA, Majors PD, Fukushima E. NMR imaging of hydrodynamics near microbially colonised surfaces. *Water Sci and Technol.* 1992;26:577–584.
13. Lewandowski Z, Altobelli SA, Fukushima E. NMR and microelectrode studies of hydrodynamics and kinetics in biofilms. *Biotechnol Progress.* 1993;9:40–45.
14. Lewandowski Z, Stoodley P, Altobelli SA, Fukushima E. Hydrodynamics and kinetics in biofilm systems—recent advances and new problems. *Water Sci and Technol.* 1994;29:223–229.
15. Lewandowski Z, Stoodley P, Altobelli SA. Experimental and conceptual studies on mass transport in biofilms. *Water Sci and Technol.* 1995;31:153–162.
16. Hoskins BC, Fevang L, Majors PD, Sharma MM, Georgiou G. Selective imaging of biofilms in porous media by NMR relaxation. *J of Magnetic Resonance.* 1999;139:67–73.
17. Nestle N, Kimmich R. Heavy metal uptake of alginate gels studied by NMR microscopy. *Colloids and Surfaces A: Physiochem and Eng Aspects.* 1996;115:141–147.
18. Nestle N, Kimmich R. NMR microscopy of heavy metal absorption in calcium alginate beads. *Appl Biochem and Biotechnol.* 1996;56:9–17.
19. Nestle N, Kimmich R. Susceptibility NMR microimaging of heavy metal uptake in alginate biosorbents. *Magnetic Resonance Imaging.* 1996;14:905–906.
20. Nestle N, Kimmich R. NMR imaging of heavy metal absorption in alginate, immobilised cells, and kombu algal biosorbents. *Biotechnol and Bioeng.* 1996;51:538–543.
21. Nott KP, Paterson-Beedle M, Macaskie LE, Hall LD. Visualisation of metal deposition in biofilm reactors by three-dimensional magnetic resonance imaging (MRI). *Biotechnol Letts.* 2001;23:1749–1757.
22. Paterson-Beedle M, Nott KP, Macaskie LE, Hall LD. Study of biofilm within a packed-bed reactor by three-dimensional magnetic resonance imaging. *Methods in Enzymology.* 2001;337:285–305.
23. Caprihan A, Fukushima E. Flow measurements by NMR. *Physics Reports.* 1990;198:195–235.
24. Pope JM, Yao S. Quantitative NMR imaging of flow, *Concepts in Magnetic Resonance.* 1993;5:281–302.
25. Fukushima E. Nuclear magnetic resonance as a tool to study flow. *Annual Reviews of Fluid Mechanics.* 1999;31:95–123.
26. Pattanapipitpaisal P, Mabbett AN, Finlay JA, Beswick AJ, Paterson-Beedle M, Essa A, Wright J, Tolley MR, Badar U, Ahmed N, Hobman JL, Brown NL, Macaskie LE. Reduction of Cr(VI) and bioaccumulation of chromium by Gram positive and Gram negative microorganisms not previously exposed to Cr-stress. *Environ Technol.* 2002;23: 731–745.
27. Allan VJM, Callow ME, Macaskie LE, Paterson-Beedle M. Effect of nutrient limitation on biofilm formation and phosphatase activity of a *Citrobacter* sp. *Microbiology.* 2002;148:277–288.
28. Xing D, Gibbs SJ, Derbyshire JA, Fordham EJ, Carpenter TA, Hall LD. Bayesian analysis for quantitative NMR flow and diffusion imaging. *J of Magnetic Resonance,* Series B. 1995;106:1–9.
29. Fogler HS. Elements of Chemical Reaction Engineering (3rd edition). New Jersey: Prentice-Hall International; 1999:882–883.
30. Yong P, Macaskie LE. Bioaccumulation of lanthanum, uranium and thorium, and use of a model system to develop a method for the biologically-mediated removal of plutonium from solution. *J of Chem Technol and Biotechnol.* 1998;71:15–26.
31. Yong P, Macaskie LE. Removal of the tetravalent actinide thorium from solution by a biocatalytic system. *J of Chem Technol and Biotechnol.* 1995;64:87–95.
32. Skoog DA, West DM, Holler FJ. Fundamentals of Analytical Chemistry (7th edition). New York: Saunders College Publishing; 1996.
33. Peters DG, Hayes JM, Hieftje GM. Chemical Separations and Measurements—Theory and Practice of Analytical Chemistry. Philadelphia: Saunders Company, 1974.
34. Yong P, Macaskie LE. Effect of substrate concentration and nitrate inhibition on product release and heavy metal removal by a *Citrobacter* sp. *Biotechnol and Bioeng.* 1997;55:821–830.

Manuscript received May 28, 2004, and revision received Feb. 25, 2005.